

## Influence of crystal planes on corrosion behavior of tantalum: Experimental and first-principles study

Yuan Luo<sup>1</sup>, Mengran Bi<sup>1</sup>, Hongzhong Cai<sup>1,\*</sup>, Changyi Hu<sup>1</sup>, Yan Wei<sup>1</sup>, Li Chen<sup>1</sup>, Zhentao Yuan<sup>2,\*</sup>, Xiao Wang<sup>2,\*</sup>

<sup>1</sup> Kunming Institute of Precious Metals, Kunming, State Key Laboratory of Advanced Technologies for Comprehensive Utilization of Platinum Metals, 650106, China;

<sup>2</sup> City College, Kunming University of Science and Technology, Kunming, 650093, China;

\*E-mail: [chz@ipm.com.cn](mailto:chz@ipm.com.cn), [kmust\\_welding@163.com](mailto:kmust_welding@163.com), [wang\\_xiao@kust.edu.cn](mailto:wang_xiao@kust.edu.cn)

Received: 9 November 2021 / Accepted: 27 December 2022 / Published: 2 February 2022

---

In order to improve the corrosion resistance of tantalum coatings produced by chemical vapor deposition (hereinafter referred to as CVD Ta) in various industrial fields, the effect of the texture on the corrosion behavior was investigated. The microstructure and electrochemical properties of CVD Ta were examined by scanning electron microscopy (SEM), X-ray diffraction (XRD), and electrochemical analysis. The surface energy and work function of the Ta surface were investigated based on first-principles calculations, which were used for the simulations of polarization curves. The SEM analysis revealed that the coatings showed a microscopic pyramid structure. Furthermore, XRD analysis results showed that the coatings mainly exhibited (110), (200), and (211) planes. Electrochemical tests showed that the coatings with a preferential orientation along the (110) plane exhibited the lowest corrosion current density value of 0.009 mA/cm<sup>2</sup> and the corrosion potential value of -0.380 V, which showed the highest quality and corrosion resistance. Further, the first-principles calculation results demonstrated that for these coatings, a highest work function and lowest surface energy result in the weakest chemical activity, which provides a theoretical explanation for the corrosion resistance corresponding to the (110) plane. Based on the results of this work, a method is proposed to regulate Cl<sub>2</sub> flow rate using consistent first-principles theory for the design and selection of Ta coatings that exhibit excellent resistance to anisotropic corrosion.

---

**Keywords:** chemical vapor deposition tantalum, selective corrosion, chlorine flow rate, first-principles calculation, simulated polarization curves.

### 1. INTRODUCTION

Corrosion resistance is an important property required in modern industrial metallic equipment and components [1,2]. Tantalum is an excellent material for applications in chemical processing

equipment because of its excellent corrosion resistance in extreme corrosive media [3,4]. The corrosion resistance and inertness of Ta are attributed to the formation of a dense and stable tantalum oxide layer on its surface [5]. However, the natural tantalum oxide layer is very thin, and the coatings quickly experience severe localized corrosion since the oxide layer is destroyed and exposed to corrosive media, resulting in the failure of coatings [6]. In theory, the crystallographic orientation of materials has a significant influence on the electrochemical activity, and the variation in the corrosion behavior cannot be the same for different planes [7,8]. Therefore, it is crucial to investigate the methods for adjusting the corrosion resistance of tantalum when the oxidation film cannot protect it from corrosive media.

Many studies have focused on increasing the oxide layer thickness and investigated the effects of crystallographic orientations [9-11]. In detail, anodic oxidation is an electrochemical technique used to increase the thickness of the oxide layer and to obtain a protective surface coating that improves anti-corrosion properties considerably [12,13]. Surface nano-crystallization is a preferred method for the control of the microstructure and texture of metals, and changing the techniques for forming the desired texture has a significant effect on the corrosion properties [14]. Deng et al. [15] and Ma et al. [16] investigated the influence of surface nano-crystallization on the formation of preferential crystallographic orientations, but the results are not entirely satisfactory because the surface nanocrystallization is not controllable. These drawbacks seriously limit the practical applications of tantalum coatings in industrial fields. Regulating the crystallographic orientation effectively solves the problems of surface nano-crystallization, but it is still difficult to control and the mechanism is not clear.

So far, considerable efforts have been made to identify the effects of crystallographic orientations on the corrosion mechanism. Xu et al. [17] found that the small layer spacing of the (211) orientation of Ta resulted in strong inter-layer interactions, which made corrosion in the case of Ta coatings with orientation along the (211) plane harder. Zhang et al. [18]. investigated the corrosion behavior of Cu along three crystal planes, and their first-principle calculation results revealed that the anti-corrosion ability was determined by the unsaturated and energetic electron of the (220) plane. Wang et al. [19] demonstrated that the {111} crystal planes of polycrystalline alloy 690 in a corrosive solution dissolve faster than the crystal faces corresponding to other orientations due to the lower surface free energy. Although these studies have deepened the understanding of the corrosion behavior of crystal Ta surfaces, the definite relationship between the crystallographic orientation and corrosion mechanism is not yet well understood. Moreover, most of these studies focused on the calculations of the surface energy and work function of different crystal planes, and discussed the relationship between the energy and the dissolution rate. The influence of resulting from the crystallographic orientation on electrochemical data was not clarified. Fortunately, Ma et al. [20] proposed a model based on the predictive theory of the anisotropic anodic dissolution of metals, which provides essential information for a more comprehensive understanding of the crystallographic corrosion of Ta.

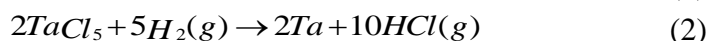
In this study, the influence of the (110), (200), and (211) crystal planes on the corrosion behavior of tantalum is investigated by performing experimental studies and first-principles calculations. Scanning electron microscopy (SEM) was employed for the surface morphology characterization, and X-ray diffraction (XRD) was used to determine the crystallographic textures of Ta coatings produced by chemical vapor deposition (hereinafter referred to as CVD Ta). Further, electrochemical analysis was performed to evaluate the corrosion caused by a 3.5% NaCl solution. First-principles calculations were

performed to investigate the influence of the work function and surface energy of Ta on different crystal planes. Notably, the polarization curves were obtained by carrying out calculations based on Tafel extrapolation using the surface energy and work function. The predicted polarization curves obtained by first-principle calculations indicate that the (110) plane has the best corrosion resistance, consistent with electrochemical results. Thus, identifying the crystal plane properties and regulating the corrosion behavior is of great significance.

## 2. EXPERIMENTAL AND COMPUTATIONAL DETAILS

### 2.1 Preparation of the CVD Ta coatings

The tantalum coatings were deposited on a Mo substrate by chemical vapor deposition (CVD) in a vertical tube reactor. Ta plates ( $\geq 99.99\%$ ) were supplied by Ningxia Orient Tantalum Industry Co. Ltd., Ningxia, China. Mo substrates (60 mm  $\times$  40 mm  $\times$  30 mm) were ultrasonically cleaned with dehydrated alcohol for 10 min and dried in a vacuum chamber.  $\text{Cl}_2$  and  $\text{H}_2$  with a purity of more than 99.9% were used.  $\text{Cl}_2$  was used as an oxidizing gas at the flow rates of 50, 100, and 150 ml/min.  $\text{H}_2$  was used as a reducing gas with a flow rate of 400 ml/min. The chlorination chamber was heated to 400 °C using an electric furnace. The substrate was kept at for 4 h 1000–1100 °C using a medium frequency induction furnace, and the total pressure was maintained at  $\sim 105$  Pa during the deposition process. After deposition, the samples were cooled to room temperature (23°C) without  $\text{H}_2$ . The total coating thickness is  $\sim 1$  mm. The substrate and the deposited coatings were separated by wire cutting and chemical etching. The main reactions that occur during the CVD process are as follows:



### 2.2 Material characterization and electrochemical measurements

The surface morphologies were studied by SEM (PhilipsXL30-ESEM). Moreover, the crystalline structure of Ta coatings was investigated by XRD (D/MAX-RC, Japan) with Cu-K $\alpha$  radiation at 200 mA and 40 kV. The  $2\theta$  values were between 10° and 100° with a step size of 0.02° and a dwell time of 1 s.

Electrochemical tests were conducted using an CHI660E workstation (CH Instruments, China) and a standard three-electrode cell. The counter electrode was composed of Pt (99.99%), and the reference electrode was a saturated calomel electrode. The surface area of CVD Ta exposed to the corrosive solution was 1 cm<sup>2</sup>. Tests were performed at the room temperature with a 3.5% NaCl solution as the electrolyte. The sample was immersed in the solution at its open circuit potential (OCP) for 3 min before measurements. Potentiodynamic polarization curves were recorded at a potential scanning rate of 0.005 V/s from  $-1.5$  V to  $+0.5$  V vs. OCP. The corrosion current density ( $I_{\text{corr}}$ ) was determined by extrapolation of the Tafel line to the corrosion potential ( $E_{\text{corr}}$ ).

### 2.3 First-principles calculation

The calculations were performed using the CASTEP code with the projector augmented wave method [21]. The ultrasoft pseudopotentials were used to study the ion-electron interactions [22]. Three models of slabs (110), (200), and (211) were prepared with five layers of atoms and vacuum range of 15 Å. The surface energy and work function were described by the Perdew–Burke–Ernzerhof generalized gradient approximation [23]. For structure optimizations, a k-point grid of  $7 \times 7 \times 1$  generated by the Monkhorst–Pack scheme was used to sample the Brillouin zone. Further, the energy cut off for the plane-wave basis was 500 eV. The energy convergence criteria and atomic force for ionic relaxations were set as  $10^{-5}$  eV and  $-0.02$  eV/Å, respectively.

## 3. RESULTS AND DISCUSSION

### 3.1 Surface morphology

Fig. 1 shows SEM images of Ta coatings deposited at different  $\text{Cl}_2$  flow rates. The microscopic surface topography exhibits a pyramidal shape without visible cracks and voids. For the  $\text{Cl}_2$  flow rate of 50 ml/min, a smooth surface was observed. With increasing  $\text{Cl}_2$  flow rate, the grain boundary becomes apparent, and the surface becomes coarse with the appearance of bigger grains. Due to the increased collision among evaporating atoms, the kinetic energy of atoms is reduced, and the diffusion rate of the adsorption atoms decreases, which favors grain growth [24]. In Fig. 1(d, e, f), the grains of all crystallites exhibit layered growth, and a layered structure becomes more obvious with the increase in the  $\text{Cl}_2$  flow rate.

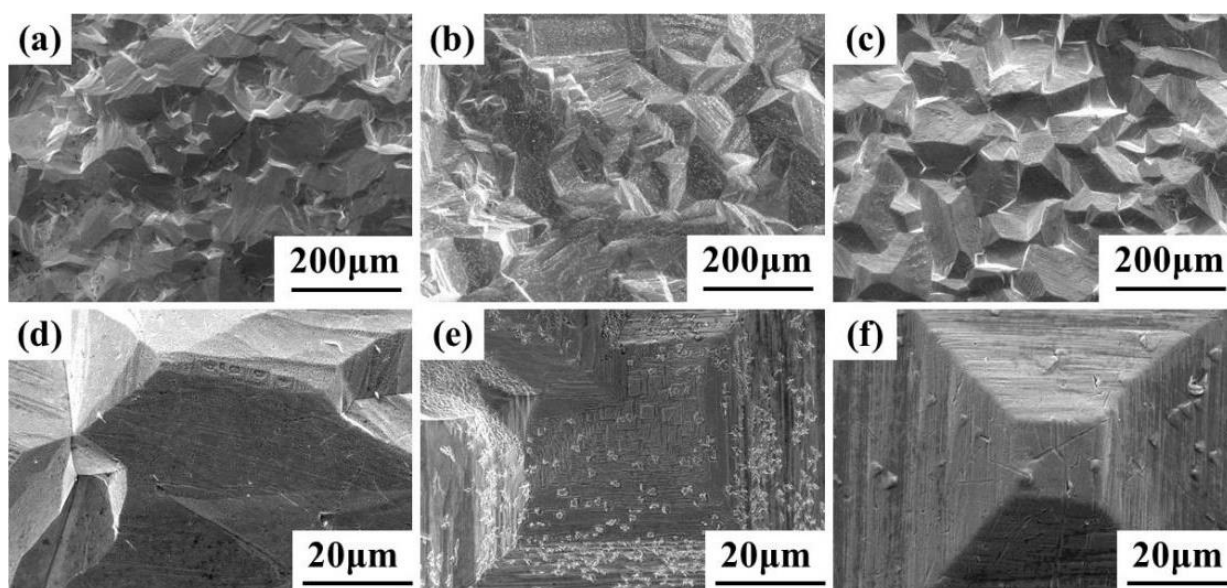


**Figure 1.** SEM images of the tantalum coatings grown at (a, d) 50, (b, e) 100, and (c, f) 150 ml/min  $\text{Cl}_2$  flow rate

### 3.2 Structural properties

In order to further determine the influence of the Cl<sub>2</sub> flow rate on the orientation of the main crystal planes of CVD Ta, the XRD pattern of the as-deposited Ta is presented in Fig. 2. Regardless of the Cl<sub>2</sub> flow rate, the coatings exhibit a crystal structure. Moreover, the coatings show three main grain orientations along (110), (200), and (211) planes. A preferential orientation along the (110) plane was observed for 50 ml/min and 100 ml/min Cl<sub>2</sub> flow rate, which is consistent with the XRD results. At 150 ml/min, the orientation along the (200) plane becomes dominant. The crystallinity was substantially improved with the increase in the Cl<sub>2</sub> flow rate, as evidenced by the higher intensity and narrower width of peaks. The higher crystallinity is caused by the movement of atoms to positions of higher stability [25]. The peak positions shift slightly from the ideal angles of diffraction, indicating a change in the interplanar spacing [26].

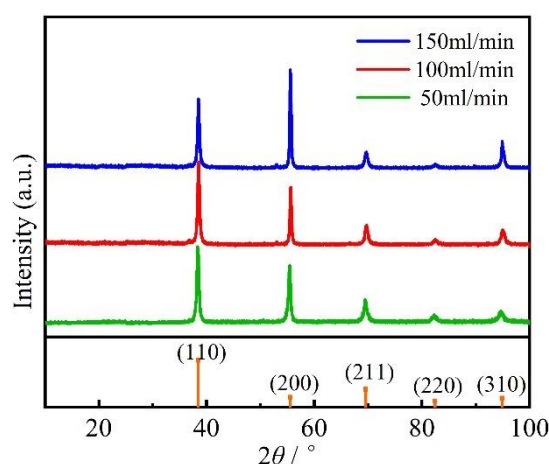


**Figure 2.** XRD pattern of Ta coatings prepared at 50, 100, and 150 ml/min Cl<sub>2</sub> flow rate

To determine the texture intensity of (110), (200), and (211) orientation, the relative intensities were obtained from XRD data and tabulated in Table 1 to calculate the texture coefficient (TC).

**Table 1.** Relative intensity determined from X-ray diffraction data for CVD Ta coating deposited at different Cl<sub>2</sub> flow rates

Crystal planes	(110)	(200)	(211)	(220)	(310)
50 ml/min	100	74	32	12	17
100 ml/min	100	70	26	9	20
150 ml/min	71	100	18	6	29
Powder	100	21	38	13	19

The TC was calculated using the Harris formula [27] and XRD results as follows:

$$TC(hkl) = \frac{I_i/I_0}{\sum_N I_i/I_0} \quad (3)$$

where  $I_i$  is the integrated intensity of different crystal plane peaks from the measured diffraction pattern,  $I_0$  is the standard intensity of the Ta powder, and  $N$  is the number of diffraction planes (in our study, only (110), (200), (211), (220), and (310) are considered, so  $N = 5$ ). The TCs corresponding to different diffraction planes are presented in Table 2.

**Table 2.** Texture coefficients of CVD Ta coating prepared at different  $\text{Cl}_2$  flow rates

Crystal planes	(110)	(200)	(211)	(220)	(310)
50 ml/min	0.139	0.490	0.117	0.129	0.125
100 ml/min	0.148	0.493	0.101	0.102	0.156
150 ml/min	0.090	0.600	0.060	0.058	0.192

The TCs corresponding to the (200) orientation at different  $\text{Cl}_2$  flow rates are always higher than those corresponding to the (110), (211), (220), and (310) orientation. A comparison of the values of TCs reveals that the TC corresponding to the (110) orientation is significantly higher at 50 ml/min and 100 ml/min  $\text{Cl}_2$  flow than at 150 ml/min. Therefore, the proportion of (110) texture of the as-deposited Ta can be adjusted by changing the  $\text{Cl}_2$  flow rate.

### 3.3 Electrochemical properties

Fig. 3 shows the anodic polarization curves for the Ta coatings in 3.5 wt.% NaCl solutions at room temperature. As shown, the as-deposited Ta gets passivated rapidly in the solution, and fluctuations of current density appear due to the nucleation and repassivation of pitting in the films with increasing potential [28]. Tafel extrapolation was carried out to determine  $E_{corr}$  and  $I_{corr}$ .  $E_{corr}$  predicts the degree of difficulty of corrosion from a thermodynamic viewpoint, and the higher the value, the less prone will the material be to corrosion. It reveals that the active dissolution range for CVD Ta was -0.380 to -0.240 V. The stable passivation behavior existed between -0.250 and -0.080 V, indicating the formation of a protective passivation film. Finally, an over-passivation region is formed between -0.080 and 0.500 V. Furthermore,  $I_{corr}$  characterizes the corrosion rate based on kinetics: the lower its value, the lower will be the metal dissolution rate and the higher will be the corrosion resistance. The corrosion parameters are tabulated Table 3. For the 50 ml/min, 100 ml/min, and 150 ml/min  $\text{Cl}_2$  flow rates, the  $I_{corr}$  values of coatings are 0.009, 0.089, and 0.018 mA/cm<sup>2</sup>, respectively.  $E_{corr}$  increases slightly with the increase in the  $\text{Cl}_2$  flow rate to -0.380, -0.379, and -0.322 V, respectively. Therefore, the lowest  $I_{corr}$  value corresponding to CVD Ta prepared with 50 ml/min  $\text{Cl}_2$  flow rate indicates the highest corrosion resistance, suggesting that the (110) plane orientation increases the anti-corrosion ability of the coatings.

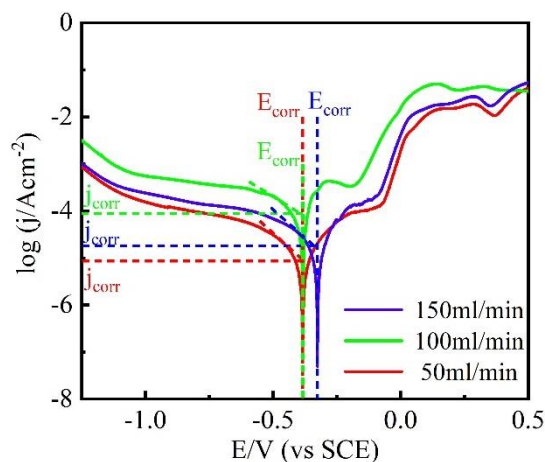


**Figure 3.** Polarization curves of CVD Ta deposited at 50, 100, and 150 ml/min  $\text{Cl}_2$  flow rate in 3.5% NaCl solution at room temperature. The potential scanning rate was 0.005 V/s

**Table 3.** Corrosion potential  $E_{corr}$  and corrosion current density  $I_{corr}$  of CVD Ta prepared at different  $\text{Cl}_2$  flow rates in 3.5% NaCl solution at room temperature

$\text{Cl}_2$ flow rates	$E_{corr} / \text{V}_{\text{SCE}}$	$I_{corr} / \text{mA} \cdot \text{cm}^{-2}$
50 ml/min	-0.380	0.009
100 ml/min	-0.379	0.089
150 ml/min	-0.322	0.018

### 3.4 First-principle calculations

#### 3.4.1 Model

Thermodynamic analysis provides a theoretical basis for predicting which chemical reactions can occur and when they will proceed until equilibrium is reached [29]. Corrosion is initiated by the provision of the energy that is needed to overcome the energy barrier between the reactants and products [30]. The initial step in corrosion is alloy dissolution, the anodic reaction occurs on the metal surface.



Metal anodic reactions involve the transfer of electrons from metal surfaces to solutions, which is initiated by the activation energy ( $\Delta G_{(hkl)}$ ) and the work done by the electric field caused by the double electric layer ( $anFU_e$ ), as shown in Fig. 4. The activation energy  $\Delta G$  is the average difference per mole between the energy of the activated particles  $G_{act}$  and that of the reactant  $G_M$  [23,29].

$$\Delta G = G_{act} - G_M \quad (5)$$

Different crystal planes have different atomic arrangements, so the total atomic energy is different, different activation energies are required during corrosion. The energy of the anode metal reactant  $G_M$  can be expressed in terms of the surface energy  $E_{surf}$ , and the relation between them is as follows [23]:

$$G_M = G_0 + N_A \times \frac{S \times E_{surf}}{N} \quad (6)$$

where  $G_0$  is the average energy per mole of the metal bulk,  $N_A$  is the Avogadro constant,  $N$  is the number of atoms on the surface,  $S$  is the surface area, and  $E_{surf}$  is the surface energy of the corresponding crystal plane.

When the metal is dissolved in the electrolyte solution, the metal atoms are converted to cations and enter the solution. Negative charges accumulate on the metal surface to form a negatively charged metal surface. There is potential attenuation between the metal surface and the solution, which finally reaches a dynamic equilibrium to form a double layer with a certain thickness. The equilibrium potential  $U_e$  between the metal surface and solution is not measurable. Therefore, the formula proposed by Trasatti [31] is introduced to calculate  $U_e$  as follows:

$$U_e = \frac{\Phi}{e} + (\Psi_M - \Psi_L) \quad (7)$$

where  $U_e$  is the equilibrium potential between the metal surface and solution,  $\Phi$  is the work function.  $\Psi_M$  and  $\Psi_L$  are the outer electric potentials of the metal (M) and solution (L), respectively, and the difference between them is the contact potential caused by an interface formed between the metal and solution [32].

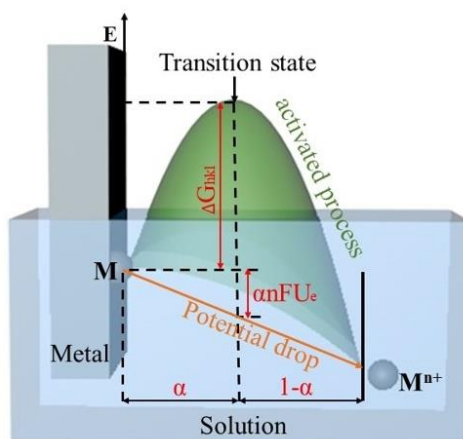


**Figure 4.** Schematic of the activation process.  $\Delta G_{(hkl)}$  is the reaction activation energy,  $anFU_e$  is the work done by the electric field in the electric double layer,  $\alpha$  is the transfer coefficient,  $n$  is the number of transferred electrons, and  $F$  is the Faraday's constant

### 3.4.2 Surface energy and work function of Ta crystallographic planes

Surface energy is the energy necessary to break the chemical bonds between atoms to form a crystal surface and can be regarded as the extra energy of the crystal surface relative to the crystal interior [33]. As a thermodynamic factor, the surface energy is very important for predicting the corrosion behavior. It can be calculated using the following equation [34]:

$$E_{surf} = \frac{1}{2S} (E_{stab} - nE_{bulk}) \quad (8)$$

where  $S$  is the area of the surface,  $E_{slab}$  is the total energy of the crystallographic planes model,  $n$  is the number of atom units of the surface, and  $E_{bulk}$  is the total energy of the perfect crystal per atom unit.

The crystal structure corresponding to the (110), (200), and (211) planes and the  $E_{surf}$  values, which are 2.326, 2.509, and 2.711 J/m<sup>2</sup>, respectively, are shown in Fig. 5. The calculated  $E_{surf}$  values reveal that the stability is in the following order: (110) > (200) > (211). The lower is the surface energy value, the higher the stability of the corresponding crystallographic planes [35], which become the preferred orientation plane in the process of crystal growth. In cases where Ta crystals are formed by CVD, (110) and (200) plane orientations are more predominant than those of (211). The calculated and experimental results of the stability trend of surfaces agree well.

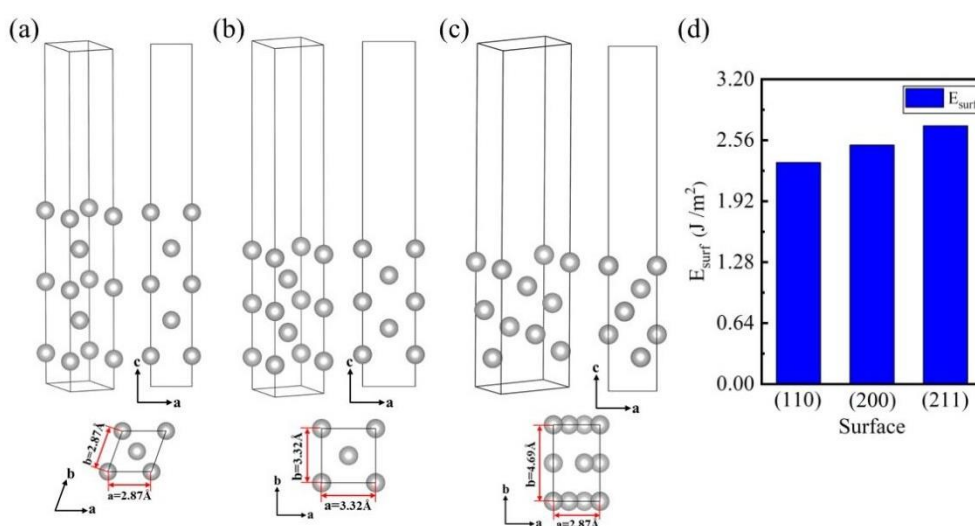


**Figure 5.** Models of (a) (110), (b) (200), and (c) (211) Ta planes for calculations and (d) computed surface energy values

The work function describes the minimum energy needed to dislodge an electron from the surface [36], which can be defined as the difference between the vacuum level energy  $E_{vac}$  and the Fermi level energy  $E_{fermi}$  [37]:

$$\Phi = E_{vac} - E_{fermi} \quad (9)$$

As presented in Fig. 6, the computed work function values for the Ta planes were found to be in the decreasing order of (110) > (200) > (211), indicating that more energy is needed to dislodge an electron from the surface in the case of the (110) plane. Therefore, the (110) plane shows higher stability in the anodic reaction.

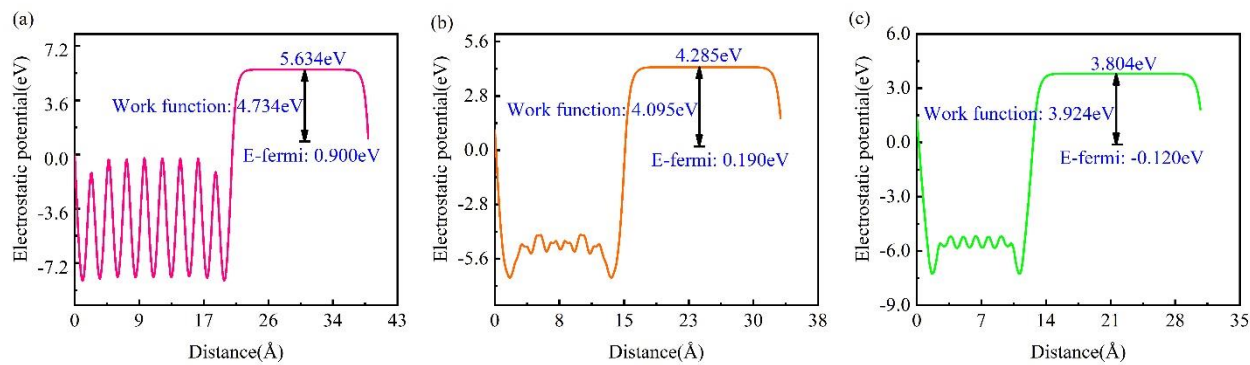


**Figure 6.** Work function of (a) (110), (b) (200), and (c) (211) Ta planes

### 3.4.3 Simulated polarization curves

In order to elucidate the corrosion-resistant behaviors corresponding to the (110), (200), and (211) crystal planes of Ta, the Tafel line of the hydrogen evolution and anodic dissolution reaction are simulated to determine the corrosion potential and corrosion current density for each plane. Ma et al. [20] proposed a systematic method for simulating the polarization curves. For the hydrogen evolution reaction, the exchange current density was assumed to be  $10^{-10}$  A/cm<sup>2</sup>, the solution pH was 11, the equilibrium potential was derived as 0.65 V vs the standard hydrogen electrode (SHE), and the value of  $\alpha$  is obtained from the slope of the Tafel curve in the experiment.

When the anodic reaction reaches equilibrium exchange, the current density  $I_0$  can be expressed as follows [20]:

$$I_0 = nF \frac{kT}{h} \exp\left(\frac{-\Delta G}{RT}\right) \times \exp\left(\frac{\alpha neU_e}{kT}\right) \times \exp\left(\frac{E_{surf} + \sum_i c_i^{vac} E_i^{vac} + \sum_j c_j^{ad} E_j^{ad}}{\rho kT}\right) \quad (10)$$

where  $n$  is the number of electrons transferred in the electrochemical reaction,  $k$  is the Boltzmann constant,  $h$  is the Planck constant,  $R$  is the gas constant, and  $T$  is the absolute temperature.  $A = 0.41$  is obtained experimentally by measuring the extrapolated Tafel slope [38].  $\rho$  is the surface atomic density:  $\rho = \frac{N}{S}$ .  $c_i^{vac}$  and  $c_j^{ad}$  are the surface vacancy concentration and adsorption concentration, respectively.

$E_i^{vac}$  and  $E_j^{ad}$  are the surface vacancy formation energy and adsorption energy [22]:

$$E_{vac} = \frac{1}{n} (E_{slab+n \times vac} - E_{slab} + nE_{bulk}) \quad (11)$$

$$E_{ad} = \frac{1}{n} (E_{ad+n \times Cl} - E_{slab} - \frac{n}{2} E_{Cl_2}) \quad (12)$$

where  $E_{slab+n \times vac}$  and  $E_{ad+n \times Cl}$  are the energies of the slab with  $n$  vacancies or Cl atoms, and  $E_{Cl_2}$  is the energy of chlorine molecule.

When the potential  $U$  between the metal surface and the solution is different from the equilibrium potential, the current density of anodic dissolution can be derived as follows [20]:

$$I = I_f - I_r = I_0 \times \left\{ \exp\left[\frac{\alpha nF(U - U_e)}{RT}\right] - \exp\left[\frac{(1 - \alpha)nF(U - U_e)}{RT}\right] \right\} \quad (13)$$

where  $I_f$  and  $I_r$  are the forward current and the reverse current, respectively.

By using Eqs. (8) and (11), the polarization curves of the (110), (200) and (211) crystal planes with (a) ideal surfaces and (b) surfaces with defects (with vacancies and adsorbed Cl) are obtained, as shown in Fig. 7.

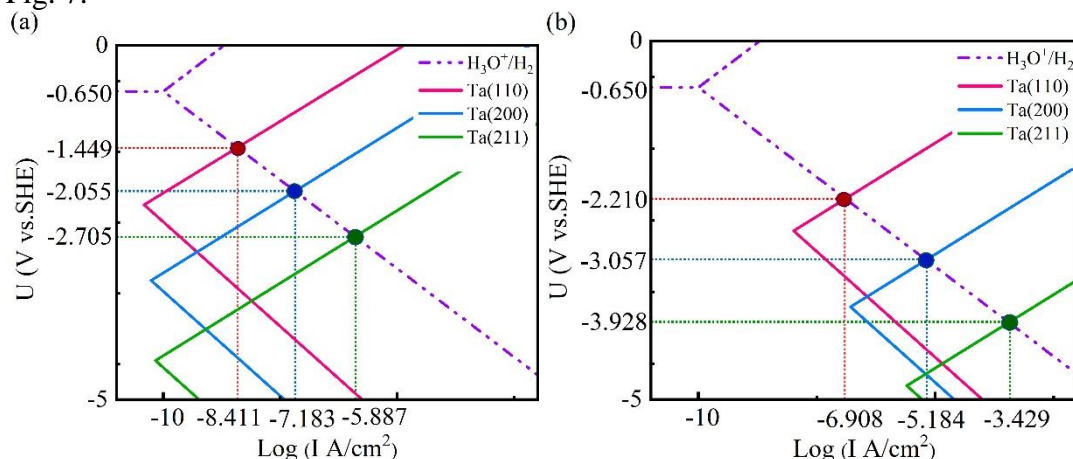


**Figure 7.** Simulated polarization curves of the anodic dissolution for the (110), (200), and (211) planes of Ta with (a) an ideal plane and (b) a plane with vacancies and adsorbed Cl

The obtained  $E_{corr}$  and  $I_{corr}$  values are determined from the intersection between the anodic curve of Ta and the cathodic curve of hydrogen. As shown in Table 4,  $E_{corr}$  of ideal and defective surfaces of crystal planes is in the following order: (110) > (200) > (211);  $I_{corr}$  decreases in the order of (211) > (200) > (110). The (110) plane with the highest  $E_{corr}$  and lowest  $I_{corr}$  dissolves slower than the other planes, confirming that it is the most stable plane, which agrees with the experimental observation. This demonstrates that the corrosion resistance is significantly different depending on the crystal orientation of pure Ta. Compared with the ideal surface, an anodic shift of the corrosion potential was observed for the defective surface: The corrosion potential deviations were  $-0.761$ ,  $-1.002$ , and  $-1.223$  V for the (110), (200), and (211) planes, respectively. The  $I_{corr}$  values reveal that the current density of the ideal surface is 2-3 orders of magnitude lower than that of the defective surface, indicating that vacancies and adsorbed chloride ions lead to higher dissolution rates. As a result, according to previous research into the corrosion behavior of CVD Ta in 3.5% NaCl, the (110) plane is the main surface of the anti-corrosion Ta.

**Table 4.** Corrosion potential  $E_{corr}$  and corrosion current density  $I_{corr}$  of the (110), (200) and (211) planes of Ta with ideal surfaces and with defective surfaces (vacancies and adsorbed Cl).

surface	Ideal surface		Defect surface	
	$E_{corr} / V$	$I_{corr} / \mu A \cdot cm^{-2}$	$E_{corr} / V$	$I_{corr} / \mu A \cdot cm^{-2}$
(110)	-1.449	$3.881 \times 10^{-3}$	-2.210	0.124
(200)	-2.055	$6.561 \times 10^{-2}$	-3.057	6.546
(211)	-2.705	1.297	-3.928	$3.724 \times 10^2$

#### 4. CONCLUSION

This study has investigated the localized corrosion of Ta by first-principles calculations to simulate the polarization curves of crystal planes. With an increase in the Cl<sub>2</sub> flow rate, the surface morphology of CVD Ta exhibits a pyramidal shape and the grains of all crystallites reveal layered growth. XRD patterns show CVD Ta growth with the (110) plane orientation as the favorable orientation at 50 ml/min and 100 ml/min Cl<sub>2</sub>, while the preferential orientation changes from the (110) to the (200) plane orientation at 150 ml/min Cl<sub>2</sub>. The electrochemical test results show that CVD Ta prepared at 50 ml/min Cl<sub>2</sub> flow rate has the lowest corrosion current density ( $I_{corr}$ ) of 0.009 mA/cm<sup>2</sup> and the self-corrosion potential ( $E_{corr}$ ) of -0.380 V, indicating that the (110) plane orientation results in the highest corrosion resistance.

By relating the surface energy and work function to simulate the polarization curves, it is found that the (110) plane with an ideal surface or with vacancies and adsorbed Cl has the highest  $E_{corr}$  of -1.449 V and -2.210 V, respectively, and the lowest  $I_{corr}$  of  $3.881 \times 10^{-3}$   $\mu\text{A}/\text{cm}^2$  and 0.124  $\mu\text{A}/\text{cm}^2$ , respectively. In particular, the surface energy decreases in the order (211) > (200) > (110), and the work function increased in the order (110) > (200) > (211). These results suggest that the high work function and low surface energy cause the weakest chemical activity, indicating that the corrosion resistance corresponding to the (110) plane is better than that corresponding to the (200) and (211) planes, which is in agreement with the experimental results.

Thus, by changing the chlorine flow rate, the surface crystal orientation can be controlled. This method is significant in that it establishes the mechanisms by which crystal planes affect the corrosion behavior and these predictions can be applied to the control of localized corrosion for Ta coatings to improve the corrosion resistance.

#### ACKNOWLEDGEMENTS

This work was supported by the National Nature Science Foundation of China (grant Nos. 52061019); Key projects of basic research plan of Yunnan Science and Technology Department (grant Nos. 202001AS070048, 202101AT070068).

#### CONFLICT OF INTEREST

We declare that we have no financial and personal relationships with other people or organizations that can inappropriately influence our work, there is no professional or other personal interest of any nature or kind in any product, service and/or company that could be construed as influencing the position presented in, or the review of, the manuscript entitled, "The influence of crystal planes on corrosion behavior of tantalum experiment and first-principles study".

#### References

1. M. Atik, S. H. Messaddeq, F. P. Luna, M. A. Aegerter. *J. Mater. Sci. Lett.*, 15 (1996) 2051.
2. A. Fattah-Alhosseini, F. R. Attarzadeh, S. Vafaeian, M. Haghshenas, M. K. Keshavarz. *Int. J. Refract. Met. H.*, 64 (2017) 168.
3. R. W. Buckman. *JOM-US*, 52 (2000) 40.

4. A. Robin, J. L. Rosa. *Int. J. Refract. Met. H.*, 18 (2000) 13.
5. H. Koivuluoto, J. Näkki, P. Vuoristo. *J. Therm. Spray Techn.*, 18 (2009) 75.
6. S. Maeng, L. Axe, T. A. Tyson, L. Gladczuk, M. Sosnowski. *Corros. Sci.*, 48 (2006) 2154.
7. X. Wang, J. A. Szpunar, L. Zhang. *Appl. Surf. Sci.*, 327 (2015) 532.
8. G. L. Song, Z. Xu. *Corros. Sci.*, 54 (2012) 97.
9. D. Prando, A. Brenna, M. P. Pedferri, M. Ormellese. *Mater. Corros.*, 69 (2018) 503.
10. J. Q. Lu, G. Y. Wei, Y. D. Yu, X. P. Zhao, Y. F. Dai. *Int. J. Electrochem. Sci.*, 12 (2017) 2763.
11. J. Chen, L. Wu, X. X. Ding, Q. Liu, X. Dai, J. F. Song, B. Jiang, A. Atrens, F. S. Pan. *J. Mater. Sci. Technol.*, 64 (2019) 10.
12. Z. Szklarska-Smialowska. *Corros. Sci.*, 33 (1992) 1193.
13. W. Simka, M. Sowa, R. P. Socha, A. Maciej, J. Michalska. *Electrochim. Acta*, 104 (2013) 518.
14. S. Wang, C. Chen, Y. L. Jia, M. P. Wang, Z. Li, Y. C. Wu. *Int. J. Refract. Met. H.*, 54 (2016) 104.
15. C. Deng, S. F. Liu, J. L. Ji, X. B. Hao, Z. Q. Zhang, Q. Liu. *J. Mater. Process. Tech.*, 214 (2014) 462.
16. G. Q. Ma, G. L. Wu, W. Shi, S. Xiang, Q. Chen, X. P. Mao. *Corros. Sci.*, 176 (2020) 108924.
17. Y. L. Xu, Z. W. Zhang, S. C. Mao, Y. Z. Ma. *Appl. Surf. Sci.*, 280 (2013) 247.
18. Z. W. Zhang, Q. Wang, X. Wang, L. Gao. *Appl. Surf. Sci.*, 396 (2017) 746.
19. S. Wang, J. Wang. *Corros. Sci.*, 85 (2014) 183.
20. H. Ma, X. Q. Chen, R. H. Li, S. L. Wang, J. H. Dong, W. Ke. *Acta Mater.*, 130 (2017) 137.
21. M. T. Gorzkowski, A. Lewera. *J. Phys. Chem. C*, 119 (2015) 18389.
22. Y. Wang, C. L. Li, H. Yang, X. Wang, J. S. Deng, X. H. Yu. *Tribol. Int.* 154 (2021) 106736.
23. C. H. Zhou, H. T. Ma, L. Wang. *Corros. Sci.*, 52 (2010) 210.
24. S. Jena, R. B. Tokas, S. Tripathi, K. D. Rao, D. V. Udupa, S. Thakur, N. K. Sahoo. *J. Alloy. Compd.*, 771 (2019) 373.
25. N. K. Oh, J. T. Kim, J. K. Ahn, G. R. Kang, S. Y. Kim, J. Y. Yun. *Appl. Sci. Conver. Tec.*, 25 (2016) 56.
26. S. Jena, R. B. Tokas, J. S. Misal, K. D. Rao, D. V. Udupa, S. Thakur, N. K. Sahoo. *Thin Solid Films*, 592 (2015) 135.
27. R. Y. Korotkov, P. Ricou, A. J. E. Farran. *Thin Solid Films*, 502 (2006) 79.
28. D. L. Zhao, C. J. Han, Y. Li, J. J. Li, K. Zhou, Q. S. Wei, J. Liu, Y. S. Shi. *J. Alloy. Compd.*, 804 (2019) 288.
29. R. C. Tolman. *J. Am. Chem. Soc.*, 42 (1920) 2506.
30. S. Q. Dong, X. Chen, E. C. La Plante, M. Gussev, K. Leonard, G. Sant. *Mater. Design*, 191 (2020) 108583.
31. S. Trasatti. *Electrochim. Acta*, 35 (1990) 269.
32. S. Trasatti. *Electrochim. Acta*, 36 (1991) 1659.
33. S. Y. Sun, S. Y. Sun, Y. Ren, X. Tan, P. P. Xu. *Surf. Interface Anal.*, 52 (2020) 167.
34. J. Andrés, L. Gracia, A. F. Gouveia, M. M. Ferrer, E. Longo. *Nanotechnology*, 26 (2015) 405703.
35. M. A. S. Khan, R. Vijayalakshmi, A. Singh, A. K. Nandi, M. B. Talawar. *CrystEngComm*, 21 (2019) 7519.
36. X. Sun, Q. Yang, R. S. Meng, C. J. Tan, Q. H. Liang, J. K. Jiang, H. Y. Ye, X. P. Chen. *Appl. Surf. Sci.*, 404 (2017) 291.
37. Z. Luo, H. Zhu, T. Ying, D. J. Li, X. Q. Zeng. *Surf. Sci.*, 672 (2018) 68.
38. G. Q. Xu, X. K. Shen, Y. Hu, P. P. Ma, K. Y. Cai. *Surf. Coat. Tech.*, 272 (2015) 58.